Submitted to the Astrophysical Journal
Preprint typeset using LaTeX style emulateapj v. 5/2/11

CAUGHT IN THE ACT: GAS AND STELLAR VELOCITY DISPERSIONS IN A FAST QUENCHING COMPACT STAR-FORMING GALAXY AT $z \sim 1.7$

Guillermo Barro[1], Sandra M. Faber[1], Avishai Dekel[2], Camilla Pacifici[3], Pablo G. Pérez-González[4], Elisa Toloba[1], David C. Koo[1], Jonathan R. Trump[5,6], Shigeki Inoue[2], Yicheng Guo[1], Fengshan Liu[7], Joel R. Primack[8], Anton M. Koekemoer[9], Gabriel Brammer[9], Antonio Cava[10], Nicolas Cardiel[4], Daniel Ceverino[11], Carmen Eliche[4], Jerome J. Fang[1], Steven L. Finkelstein[12], Dale D. Kocevski[13], Rachael C. Livermore[12], Elizabeth McGrath[13]

Submitted to the Astrophysical Journal

ABSTRACT

We present Keck-I MOSFIRE spectroscopy in the Y and H bands of GDN-8231, a massive, compact, star-forming galaxy (SFG) at a redshift $z \sim 1.7$. Its spectrum reveals both Hα and [N II] emission lines and strong Balmer absorption lines. The Hα and *Spitzer* MIPS 24 μm fluxes are both weak, thus indicating a low star formation rate of SFR $\lesssim 5-10$ M$_{\odot}$ y^{-1}. This, added to a relatively young age of ~ 700 Myr measured from the absorption lines, provides the first direct evidence for a distant galaxy being caught in the act of rapidly shutting down its star formation. Such quenching allows GDN-8231 to become a compact, quiescent galaxy, similar to 3 other galaxies in our sample, by $z \sim 1.5$. Moreover, the color profile of GDN-8231 shows a bluer center, consistent with the predictions of recent simulations for an early phase of inside-out quenching. Its line-of-sight velocity dispersion for the gas, $\sigma^{\rm gas}_{\rm LOS} = 127 \pm 32$ km s^{-1}, is nearly 40% smaller than that of its stars, $\sigma^{\star}_{\rm LOS} = 215 \pm 35$ km s^{-1}. High-resolution hydro-simulations of galaxies explain such apparently colder gas kinematics of up to a factor of ~ 1.5 with rotating disks being viewed at different inclinations and/or centrally concentrated star-forming regions. A clear prediction is that their compact, quiescent descendants preserve some remnant rotation from their star-forming progenitors.

Subject headings: galaxies: photometry — galaxies: high-redshift

1. INTRODUCTION

The formation and structural evolution of the first quiescent galaxies at $z \gtrsim 2$ has been the subject of considerable discussion in recent years. Since the first papers reporting their remarkably compact nature compared to quiescent galaxies of similar stellar mass at low redshift, many studies have verified their small sizes and characterized its growth with cosmic time (Daddi et al. 2005; Trujillo et al. 2007; Buitrago et al. 2008; Cimatti et al. 2008; van Dokkum et al. 2008; Damjanov et al. 2009; Cassata et al. 2011; Szomoru et al. 2012; Newman et al. 2012a; Carollo et al. 2013; van der Wel et al. 2014). However, the mechanisms responsible for the formation of such compact objects are still unclear.

A crucial step forward in understanding these formation processes is the recent discovery of a population of massive (log(M/M$_{\odot}$)>10), compact star-forming galaxies at $z \gtrsim 2$ (Wuyts et al. 2011b; Barro et al. 2013, 2014a; Patel et al. 2013; Stefanon et al. 2013). These galaxies have similar structural properties to the compact quiescent population, i.e., spheroidal morphologies, centrally concentrated luminosity profiles and high Sérsic indices. The similar properties and number densities suggest that these compact star-forming galaxies (SFGs) are the immediate progenitors of the similarly compact first quiescent galaxies (Barro et al. 2013). Compact SFGs are typically found in a dusty star-forming phase characterized by bright far-IR and sub-mm detections, and relatively *normal* star formation rates (SFRs) similar to those of other star-forming galaxies of the same mass and redshift, in what is usually referred to as the star-forming main sequence (Noeske et al. 2007; Elbaz et al. 2007; Salim et al. 2007; Pannella et al. 2009; Magdis et al. 2010; Wuyts et al. 2011a; Elbaz et al. 2011; Rodighiero et al. 2010; Whitaker et al. 2012b; Pannella et al. 2014). However, they have radically different morphologies suggesting that their compact nature is the result of strongly dissipative transformation processes, such as mergers (Hopkins et al. 2006; Naab et al. 2007; Wuyts et al. 2010; Wellons et al. 2014) or accretion-driven disk instabilities (Dekel et al. 2009; Ceverino et al. 2010; Dekel & Burkert 2014; Zolotov et al. 2014) that funnel a large fraction of their gas reservoirs into the center, rapidly building up a dense stellar core.

Additional evidence in support of the evolutionary connection between compact SFGs and quiescent galaxies came recently when NIR spectroscopy of a sample of compact SFGs revealed emission line widths of $\sigma = 200-300$ km s^{-1} (Barro et al. 2014b; Nelson et al. 2014), in good agreement with the observed stellar velocity dispersions of compact quiescent galaxies of similar stellar mass (Newman et al. 2010; van de Sande et al. 2013; Bezanson et al. 2013; Belli et al. 2014b). However,

[1] University of California, Santa Cruz
[2] The Hebrew University
[3] Yonsei University Observatory
[4] Universidad Complutense de Madrid
[5] Pennsylvania State University
[6] Hubble Fellow
[7] Shenyang Normal University
[8] Santa Cruz Institute for Particle Physics
[9] Space Telescope Science Institute
[10] Observatoire de Geneve
[11] Centro de Astrobiologia, CSIC-INTA
[12] The University of Texas at Austin
[13] Colby College

these measurements are based on different dynamical tracers, and measured on disjoint populations. Therefore the implied evolutionary connection between them is indirect. Some caveats to this evolutionary sequence are, for example: 1) the broad emission lines may be driven by shocks and outflows rather than the gravitational potential (Newman et al. 2012b; Genzel et al. 2014) , and 2) if compact SFGs do not quench immediately, their current dynamics may have little to do with their eventual transition into quiescent galaxies.

A way forward to address these issues is to study the properties of both the gas and the stars on the same galaxies. These kinematic properties can be used to test whether the gas and the stars are probing the same gravitational potential, and the simultaneous measurement of emission and absorption lines can be used to estimate the age and star-formation history (SFH) of their stellar populations. However, these kind of measurements, are still observationally challenging, particularly for galaxies at $z \gtrsim 1.5$. Firstly, absorption line measurements (e.g., the Balmer or the CaHK lines) require NIR spectrographs and long (>8 hr) integrations on $8-10$ m class telescopes, and probing the stronger emission lines (e.g., H$\alpha\lambda$6563 Å, [N II]λ6584 Å, [O III]λ5007 Å, H$\beta\lambda$4861 Å) on the same galaxies often requires additional observations in other bands. Secondly, the spectra of galaxies are typically dominated by either emission or absorption lines, and the phases in which both sets of lines are strong are usually short and depend on the SFH of the galaxy.

Interestingly, several papers have identified a substantial population of recently quenched (i.e., young) compact quiescent galaxies at $z \gtrsim 1.5$ which are the most promising candidates to have both absorption lines from an old, underlying population, and emission lines from weak, residual star-formation (Newman et al. 2010; van Dokkum & Brammer 2010; Toft et al. 2012; Onodera et al. 2012; van de Sande et al. 2013; Bezanson et al. 2013; Bedregal et al. 2013; Belli et al. 2014a,b). Spectroscopic follow-up of these galaxies have revealed prominent Balmer absorption lines and, occasionally, emission in [O II]. The [O II]$\lambda 3726+3729$ doublet, however, is typically unresolved at the resolution of these observations, and thus it is not a reliable kinematic indicator. Additional observations of these galaxies for other emission lines in the Hα or [O III] ranges have so far been unsuccessful.

In this paper, we present Y and H band spectroscopy of a massive ($\log(M/M_\odot) = 10.75$), compact SFG at $z = 1.674$ obtained with the MOSFIRE multi-object infrared spectrograph (McLean et al. 2010; McLean et al. 2012) on the Keck-I telescope. The spectra of GDN-8231 show emission and absorption lines which suggest that the galaxy is quenching rapidly. We model these lines to estimate the kinematics of the gas and the stars. In addition, we combine the spectra with optical medium-band photometry from the SHARDS survey (Pérez-González et al. 2013) and Hubble Space Telescope (*HST*) WFC3 grism spectroscopy in G102 (GO13420; PI=Barro) and G141 (GO11600; PI=Weiner) to obtain detailed spectral energy distributions (SEDs) for the quenching galaxy and 3 older quiescent galaxies, observed as a part of the same MOSFIRE survey. From the modeling of their SEDs, we estimate their stellar ages and SFHs, and analyze the implications for the evolutionary path from compact SFG to compact quiescent galaxy.

Throughout the paper, we adopt a flat cosmology with Ω_M=0.3, Ω_Λ=0.7 and $H_0 = 70$ km s^{-1} Mpc^{-1} and we quote magnitudes in the AB system.

2. DATA

2.1. *Target Selection*

We select spectroscopic targets from the CANDELS (Grogin et al. 2011; Koekemoer et al. 2011) WFC3/F160W (H band) multi-wavelength catalogs in GOODS-N (Barro et al. in prep.). This catalog includes deep, UV-to-NIR ground-based observations in several medium and broad bands, *HST* photometry in 9 different bands and *Spitzer*/*Herschel* observations in the mid-to-far IR. The source extraction and merged multi-wavelength spectral energy distributions (SEDs) are measured following the procedures described in Galametz et al. (2013) and Guo et al. (2013). In addition, GOODS-N includes complementary *HST*/WFC3 observations in both G102 and G141 grisms, allowing for continuous wavelength coverage from $0.9 < \lambda < 1.7$ μm with a resolution better than R= 130 (e.g., Brammer et al. 2012). The grism data are reduced using the threedhst[14] pipeline. The pipeline handles the combination and reduction of the dithered exposures, and the extraction of the individual spectra. These are background subtracted and corrected for contamination from the overlapping spectra of nearby sources (Brammer et al. 2012; Momcheva et al. in prep). The grism data are joined at shorter wavelengths by the 25 optical medium-bands of the SHARDS survey ($R \sim 50$; Pérez-González et al. 2013). Together, these datasets provide remarkable spectral resolution on a galaxy-by-galaxy basis, that is uniquely suited for SED-fitting analysis (see § 3). The stellar masses, rest-frame colors, and photometric redshifts used for target selection are derived via SED-fitting using EAzY (Brammer et al. 2008) and FAST (Kriek et al. 2009), assuming Bruzual & Charlot (2003) stellar population synthesis models, a Chabrier (2003) initial mass function (IMF), and the Calzetti et al. (2000) dust extinction law. The SFRs are computed by adding the unobscured and obscured star formation, traced by the UV and IR emission, following the method described in Wuyts et al. (2011a, see also Barro et al. 2013, 2014a)

We select galaxies in a *transition* stage between the star-forming main sequence and the quiescent, red sequence using $-0.75 < \log(\mathrm{sSFR/Gyr^{-1}}) < -0.25$. This corresponds to galaxies approximately $\sim 2\sigma$ below the main sequence at $z \sim 1.75$ (Whitaker et al. 2012b). For galaxies with $\log(M/M_\odot) > 10$, this threshold roughly corresponds to a SFR $\gtrsim 10$ $M_\odot$ y^{-1}, which is the 5σ detection level with MOSFIRE in $\sim$1h exposures (e.g., Trump et al. 2013; Kriek et al. 2014). We also impose the compactness criterion of Barro et al. (2013), $M/r_e^{1.5} = 10.3$ $M_\odot$kpc$^{-1.5}$, to select galaxies with similar structural and morphological properties as the quiescent population at that redshift. Figure 1 illustrates that the sSFR criterion is consistent with the $U-V$ vs.

[15] http://code.google.com/p/threedhst

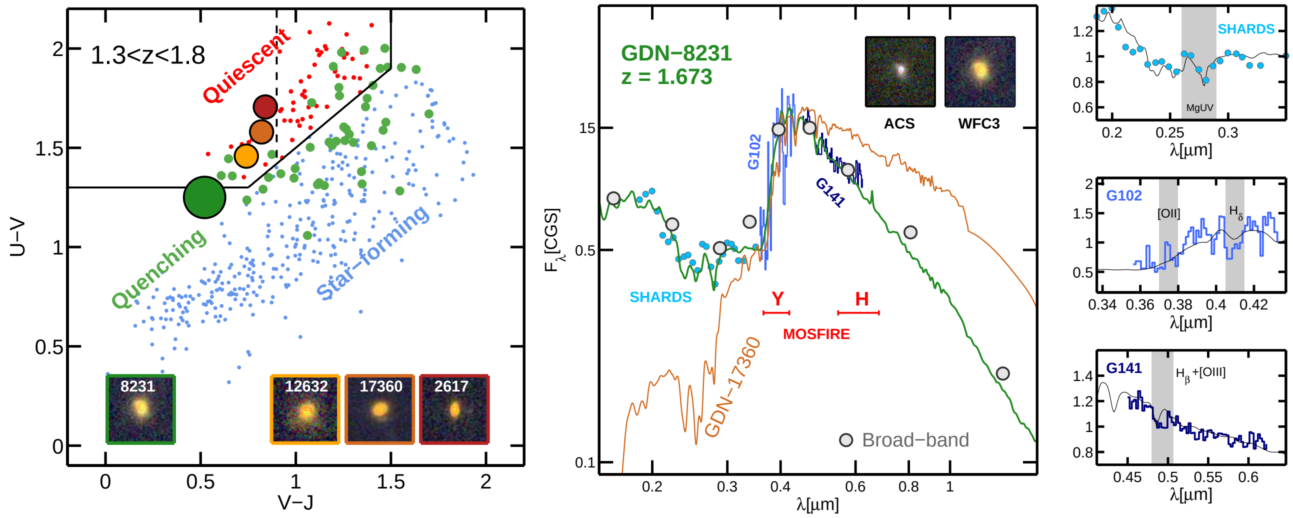

FIG. 1.— *Left panel:* UVJ diagram for galaxies at $1.3 < z < 1.8$ more massive than $\log(M/M_\odot) > 10$ in the GOODS-N field. The colors highlight different populations of star-forming galaxies (blue; $\log(sSFR/Gyr^{-1}) > -0.25$), quiescent galaxies (red; $\log(sSFR/Gyr^{-1}) < -0.75$) and quenching, transition, galaxies (green; $-0.25 < \log(sSFR/Gyr^{-1}) < -0.75$) identified according to their UV+IR SFRs. The large markers show the quenching, compact SFG (GDN-8231; dark green) and the 3 quenched galaxies (GDN-2617, 17360, 12632; orange to red) observed with MOSFIRE. The *HST* color images (zJH) of the 4 galaxies are shown at the bottom. The location of GDN-8231 in the UVJ is consistent with the observed spectral and photometric properties, indicating that it is a weakly star-forming galaxy transitioning to a quiescent phase. The quiescent galaxies fall within the selection region for recently quenched galaxies (left of the dashed line; Whitaker et al. 2012a). *Right panel:* Color images (ACS and WFC3), and composite SED of GDN-8231. The grey circles show the (low-resolution) broad-band photometry, the cyan markers show the SHARDS medium-band data (R∼ 50;Pérez-González et al. 2013) and the light and dark blue lines show the *HST*/WFC3 G102 and G141 grism spectra. The spectral regions probed by Y and H band MOSFIRE spectra are indicated in red. The green and orange lines show the best-fit stellar population templates from Pacifici et al. (2012) at a resolution of R= 50 for GDN-8231 and the quiescent galaxy GDN-17360. The 3 sub-panels on the right show the zoom-in around the SHARDS, G102 and G141 data highlighting spectral features in Mg_{UV}, [O II], Hδ and Hβ.

$V-J$ (hereafter UVJ) rest-frame color criterion that has been shown to be very successful in identifying quiescent galaxies, breaking the age/dust degeneracy (Wuyts et al. 2007; Williams et al. 2010; Whitaker et al. 2011). The spread of the *transition* sample along the wedge of the UVJ quiescent region is primarily driven by differences in the dust reddening and in the stellar population ages, which suggests a wide diversity of extinction levels and SFHs among quenching galaxies (e.g., Wild et al. 2014).

We select the most promising candidates for spectroscopic follow-up by prioritizing bright galaxies with low dust reddening to maximize the signal-to-noise (S/N) ratio. This additional restriction preferentially selects galaxies with bluer UVJ colors, near the so-called post-starburst region of the UVJ diagram (left of the dashed line in Figure 1; Whitaker et al. 2011; Bezanson et al. 2013). This region encompasses colors that are typical of recently quenched galaxies, with low extinction levels and young stellar ages of $\lesssim 1$ Gyr. Galaxies in this region also have, on average, lower stellar masses ($\log(M/M_\odot) \lesssim 10.8$) than older quiescent galaxies with redder colors (Newman et al. 2013; Barro et al. 2014a).

The redshift is restricted to the range $1.3 < z < 1.8$ that places the Hα emission line in the H band and several other Balmer lines around the 4000 Å break in the Y band. The observed mask contains 1 candidate that is a *transitioning*, compact SFG (GDN-8231; green circle) and 3 recently quenched galaxies (GDN-12632, GDN-17360 and GDN-2617; orange to red circles). GDN-8231 is relatively massive ($\log(M/M_\odot) = 10.7$) and presents low levels of star-formation (SFR $= 10$ $M_\odot$ y^{-1}) evidenced by a weak detection in MIPS 24 μm ($f(24) = 40$ μJy). The low sSFR and mild extinction ($A_V = 0.3$ mag) are consistent with its location in the UVJ diagram, and suggests that it is on the brink of becoming a young quiescent galaxy, similar to the 3 quiescent targets in our sample. The photometric and spectroscopic galaxy properties of the four galaxies are summarized in Table 1.

2.2. *Spectroscopic data*

Data were collected on the nights of 2014 April 17 and May 11 using the MOSFIRE instrument (McLean et al. 2010, 2012) on the Keck-I telescope. The sky conditions were clear and the median seeing ranged from $0.''5 - 0.''7$ seeing. We observed 1 mask configuration in both the Y ($0.97 < \lambda < 1.12$ μm) and H bands ($1.46 < \lambda < 1.81$ μm), with individual exposure times of 180 s and 120 s, for a total 5.5 h and 2 h, respectively. We used 2-point dithers separated by $1.''5$ and slit widths of $0.''7$. The instrumental resolution of MOSFIRE with $0.''7$ slit widths is approximately $R = 3200$ (∼5 Å per resolution element). The 2D spectra were reduced, sky subtracted, wavelength calibrated, and one-dimensionally extracted using the public MOSFIRE data reduction pipeline[16].

3. ANALYSIS

3.1. *Kinematic measurements and line ratios*

The 4 galaxies are NIR bright ($H < 22$ mag) and present clear continuum detections (S/N> 5) in both the Y and H band spectra. GDN-8231 exhibits multiple Balmer absorption lines in the Y band spectrum, from Hδ to H10, and it is the only galaxy showing Hα and [N II] emission lines in the H band spectrum (Figure 2).

[17] `http://www2.keck.hawaii.edu/inst/mosfire/drp.html`

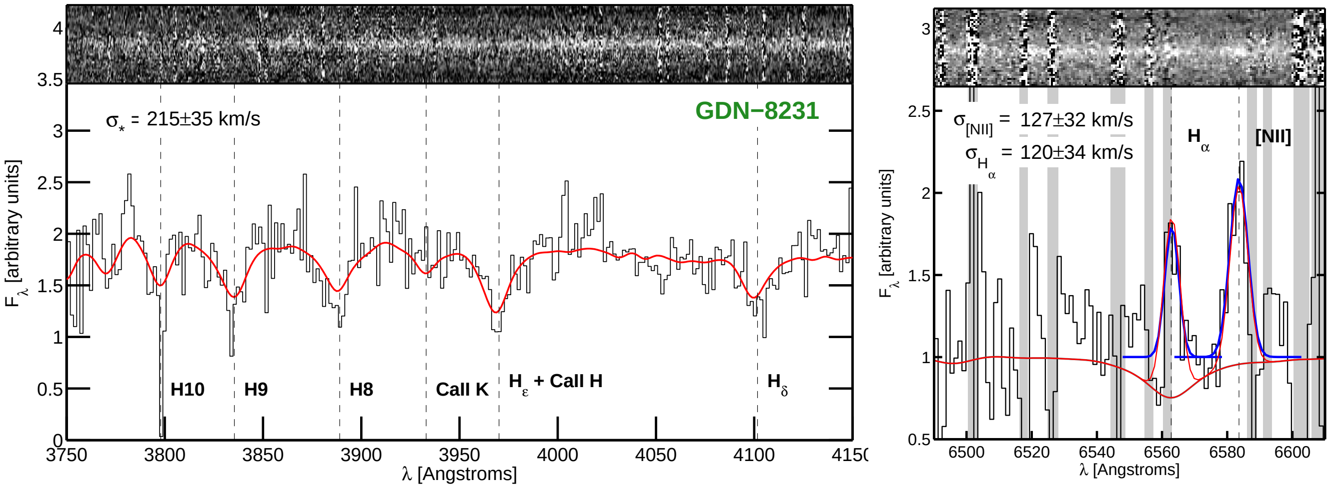

FIG. 2.— *Left panel:* MOSFIRE Y band spectrum of the quenching, compact SFG (GDN-8231) with detected absorption lines. The best-fit model used to determine the stellar velocity dispersion and the absorption indices is shown in red. *Right panel:* MOSFIRE H band spectrum of GDN-8231 showing the spectral range around the Hα and [N II] lines. The regions contaminated by sky lines are shown in gray. The blue Gaussians show the best fit to the Hα ($\sigma_{\rm LOS}$ = 97 km s^{-1}) and [N II] ($\sigma_{\rm LOS}$ = 127 km s^{-1}) lines using the average continuum level. The red Gaussians show the best-fit to the Hα line ($\sigma_{\rm LOS}$ = 120 km s^{-1}) correcting for the Hα stellar absorption as determined from the fit to the Y band spectrum.

The other 3 quiescent galaxies also have clear Balmer absorption lines in the Y band but present no emission lines in the H band.

We measure the line-of-sight (LOS) stellar velocity dispersion using the penalized pixel-fitting software pPXF (Cappellari & Emsellem 2004). This software fits the galaxy spectrum with a model created as a linear combination of the stellar templates that best reproduce the galaxy spectrum allowing different weights for each templates. The stellar templates used are the stars from the MILES stellar library (Sánchez-Blázquez et al. 2006b; Cenarro et al. 2007). Before fitting the galaxy spectrum, we mask the regions contaminated by telluric atmospheric bands and pixels with strong residuals from the sky lines, and convolve it with a Gaussian function whose width is the quadratic difference between the resolution of the MILES stellar library (FWHM = 2.5 Å; Falcón-Barroso et al. 2011) and the instrumental resolution of our observations measured in sky lines (FWHM = 2.7 Å). We estimate the uncertainty in the stellar velocity dispersion by running 1000 Monte Carlo simulations. In each simulation, the flux of the spectrum is perturbed within a Gaussian function whose width is the uncertainty in the flux obtained in the reduction process. The stellar velocity dispersion is measured in each simulation and the uncertainty is the standard deviation of the Gaussian distribution of all 1000 velocity dispersion estimates. Based on this method, we obtain a stellar velocity dispersion for GDN-8231 of $\sigma^{\star}_{\rm LOS} = 215 \pm 35$ km s^{-1} (see Table 1 for the quiescent galaxies).

We measure the LOS gas velocity dispersion, $\sigma^{\rm gas}_{\rm LOS}$, of GDN-8231 by fitting a Gaussian profile to the emission lines, measuring its FWHM, and subtracting the instrumental broadening in quadrature from the FWHM. The velocity dispersion is then the corrected FWHM divided by 2.355. We fit the Hα and [N II] lines independently. As shown in Figure 2, [N II] is detected at higher S/N ratio because the Hα line is partially contaminated by a skyline, and it appears to be self-absorbed (i.e., the continuum emission is affected by Balmer absorption). As a result, if we fit the lines using the same continuum level the velocity dispersion inferred from Hα is smaller than that from [N II], $\sigma^{\rm gas}_{\rm LOS} = 90 \pm 18$ km s^{-1} and 127 ± 32 km s^{-1}, respectively. Although it is possible for Balmer and forbidden lines to have different widths if they originate in different regions, the most likely explanation for such a large difference is the self-absorption in Hα. To account for that effect, we use the best-fit stellar template to the absorption spectra to establish the continuum level for the Hα emission, and we recompute the fit. With this method, the inferred velocity dispersion is $\sigma^{\rm gas}_{\rm LOS} = 120 \pm 34$ km s^{-1}, consistent with the [N II] result. Although the two measurements agree after accounting for Balmer absorption, we adopt the higher-S/N [N II] measurement as the more reliable tracer of gas velocity dispersion.

The spectra are not flux calibrated. However, we can use the equivalent width of Hα corrected for stellar absorption (EW(Hα)$_{\rm corr}$ = 8.3 ± 0.7) and the continuum flux, inferred from the SED modeling, to calculate the Hα line flux and SFR. Using the empirical relation from Kennicutt (1998) and the attenuation inferred from SED-fitting ($A_V = 0.3$), we obtain values of SFR = $3 - 6$ $M_\odot$ y^{-1}, depending on the extra nebular extinction with respect to the continuum ($A_{H\alpha} = 2.44 - 1.86\ A_{\rm cont}$; e.g., Calzetti et al. 2000; Price et al. 2014). These values are consistent with the estimate from MIPS 24 μm data. The Hα line flux corrected for stellar absorption also allows us to estimate the intrinsic value of the line ratio [N II]/Hα= 1.2. Even without measuring the [O III]/Hβ line ratio to fully constrain the ionization diagnostic diagram (i.e., BPT; Baldwin et al. 1981), an [N II]/Hα ratio of the order of unity already suggests that the nebular emission is at least partially powered by an AGN. The galaxy, however, is not detected in the 2Ms X-ray data (Alexander et al. 2003) which implies that the AGN is relatively weak, perhaps shutting down along with the star formation in the galaxy. This result, together with the large fraction of AGNs ($\sim$ 40%) found in compact SFGs at $z = 2-3$ (Barro et al.

2014a), suggest that the black hole growth at high redshift closely follows the star-formation history (i.e., it starts and shuts down with the star-formation), as opposed to the observed trend in the local Universe, where there seems be to a delay between the starburst and the peak of the AGN phase (Wild et al. 2010; Yesuf et al. 2014; Hernán-Caballero et al. 2014). In that case, AGN may play a more active role in the quenching of star formation at $z \sim 2$.

3.2. *Luminosity profile and Morphology*

The MOSFIRE spectra of GDN-8231 are spatially unresolved and thus do not provide additional insights on the kinematic profile of the gas and the stars, or the spatial distribution of star formation. The high-resolution *HST* imaging, however can be used to determine the overall structural properties and the radial distribution of star-formation in the galaxy. Figure 3 shows the surface brightness and color profiles of GDN-8231 computed from the fitting of the HST-based SEDs measured at each radius. The profile shows a positive color gradient of $d(NUV-V)/dr = 6 \cdot 10^{-3}$ mag/kpc that is indicated by a bluer center with a 20% smaller r_e in the rest-frame NUV with respect to the V band ($r_{e,NUV}/r_{e,V} = 0.8$). Assuming that the NUV is a good tracer of the SFR, these measurements suggest that the SFR profile is more centrally-concentrated than the stellar profile. A possible interpretation for this result is that we are witnessing the quenching of a central starburst right after it has formed a dense stellar core ($\Sigma_{1\ \rm kpc}$ = 9.7 $M_\odot$ kpc^{-2}), which seems to be a pre-requisite for quiescent galaxies (Cheung et al. 2012; Fang et al. 2013; van Dokkum et al. 2014). Such interpretation is an excellent match for the predictions of simulations that describe the formation of compact galaxies as the result of strongly dissipative gas-rich events, such as mergers and/or disk instabilities (e.g., Dekel & Burkert 2014; Zolotov et al. 2014; Wellons et al. 2014). These processes are characterized by a wet-inflow (i.e., gas-inflow rate > SFR) that builds-up the central gas density, thereby enhancing the SFR at the center and growing a dense stellar core. The weakening of such inflow marks the onset of inside-out quenching due to gas depletion. In that onset phase, the SFR is still high and thus the color gradient is still positive, as observed in GDN-8231. However, as inside-out quenching progresses, the SFR profile flattens, and the color gradient turns negative, as observed in compact quiescent galaxies (Guo et al. 2012; **?**; Szomoru et al. 2012).

GDN-8231 has high-Sérsic values consistent with other compact star-forming and quiescent galaxies (Barro et al. 2013). Its visual appearance in the *H* band is smooth and spheroidal. However, the ACS images, that probe the rest-frame UV, show small irregular patches, perhaps indicative of its prior, dissipative compaction event. Adopting the assumptions of Miller et al. (2011), we infer a viewing-angle inclination of $i = 42°$ from an axis-ratio value of $b/a = 0.74$.

3.3. *Spectral indices and SED fitting*

One of the main obstacles to estimating stellar population properties from the analysis of SEDs is that at the typical resolution of broad-band surveys

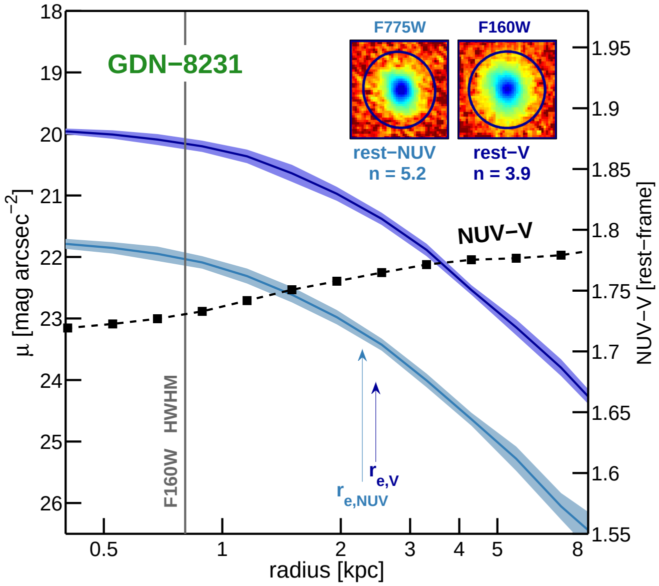

Fig. 3.— Rest-frame surface brightness profile and color profile of GDN-8231. The rest-frame profiles are computed by interpolating at each radius the best-fit SED derived from the observed surface brightness profile in 9 HST bands measured with IRAF/ellipse (see Liu et al. 2013 and Liu et al. in prep for more details). At z = 1.67, the rest-frame NUV and V bands roughly correspond with the observed i and H bands, respectively. The arrows indicate the effective radius in those bands from the best-fit Sérsic profiles obtained using GALFIT. The grey line indicates the PSF half width at half-maximum (HWHM) in the H band. The insets show the images of GDN-8231 in the i (PSF-matched to H band) and H bands. The black circle has radius of 1″(∼ 8.4 kpc). GDN-8231 has an positive color gradient and relatively low sSFR, which are consistent with the expectations for an early phase of inside-out quenching after a central starburst.

(FWHM∼0.2 μm/(1+z); R∼6) the most relevant continuum and emission/absorption line features are usually diluted, which results in large uncertainties in inferred properties (Muzzin et al. 2009; Conroy & Gunn 2010). One way to circumvent this problem is by using higher spectral resolution data to obtain more accurate measurements of line strengths and spectral indices, which are key indicators of stellar age, and present/past star-formation activity (e.g., Kelson et al. 2001; Kauffmann et al. 2003).

From the MOSFIRE Y band spectra we measure the H$\delta_{\rm A}$ Lick index (Worthey & Ottaviani 1997) using PPXF to estimate the best-fit value and uncertainty. This index has been traditionally used as an age and SFH indicator (Trager et al. 2000; Sánchez-Blázquez et al. 2006a). From the H band spectra we measure the Hα Equivalent Width, EW(Hα), which is sensitive to the instantaneous (last few Myr) SFR. Only GDN-8231 presents Hα emission, the other 3 quiescent galaxies have strong continuum detections that place reliable upper limits on EW(Hα). In addition to the MOSFIRE spectra, we use the SHARDS medium-band data and the *HST* grism data to probe for additional absorption features and continuum breaks. The right panel of Figure 1 illustrates the high spectral resolution (∼ $10-100\times$ better than broad-band filters) of the merged medium-band/grism SED, revealing Mg II absorption at 2800 Å in SHARDS and Balmer absorption lines and the 4000 Å break in G102 and G141. We quantify the later using the D4000 index (e.g., Balogh et al. 1999;

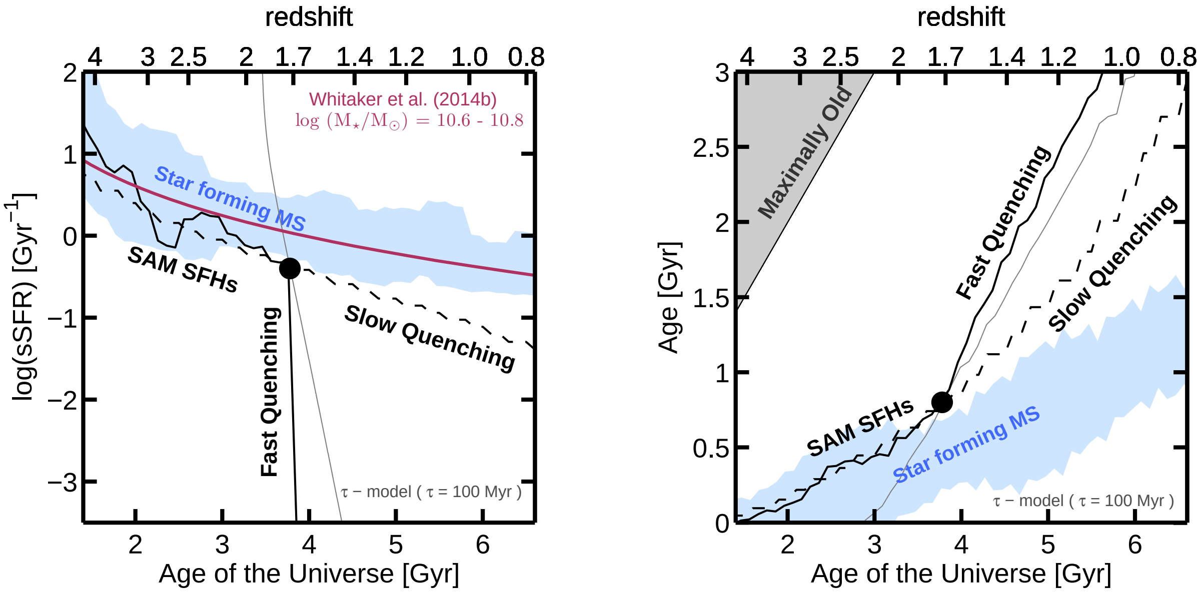

FIG. 4.— Evolutionary tracks in sSFR (left) and luminosity-weighted age (right) vs. age of the Universe for different SFHs. The blue shaded region depicts the star-forming main sequence determined from the average SFH of SFGs drawn from the model library of Pacifici et al. (2012). This region agrees well with the observational results of Whitaker et al. (2014) for SFGs of intermediate mass. The black lines illustrate the evolution of 2 galaxies that have a secular growth from $z \sim 4$ to $z = 1.7$, followed by either fast (solid) or slow (dashed) quenching of star formation. In a fast quenching galaxy the luminosity-weighed age grows linearly with time (passive evolution). However, in a slow quenching (or main sequence) galaxy the luminosity-weighed age increases more slowly (i.e., the slope is < 1). A τ model can describe either a fast or slow quenching. However, a short τ (gray line) would provide unrealistic results for galaxies described by a two-phase SFH (e.g., a main sequence + fast quenching).

Kauffmann et al. 2003). The G102 grism shows also a weak [O II] emission line (EW 15 ± 5 Å). However, there is no clear sign of [O III] emission in G141. The later is expected to have also low EW $\lesssim 10$ Å, and thus can be partially hidden by the Hβ absorption, as hinted in the stacked spectra of recently quenched galaxies in Whitaker et al. (2013).

The spectral indices are usually analyzed by comparing measurements to a grid of values derived from stellar population synthesis models. Here we follow a slightly different approach to combine information from both the indices and the overall UV-to-NIR SED by using of the SED-fitting code of Pacifici et al. (2012, hereafter P12). The code performs a simultaneous fitting of the low and high resolution data and includes priors on the EW of emission and absorption lines to obtain better constraints on the SFR and SFH of the galaxy (see also Pacifici et al. 2014, 2015 and Barro et al. 2014a for more details). The galaxy templates are computed from non-parametric SFHs adapted from semi-analytic models (SAMs) and include both the stellar continuum and the nebular emission. The SAM SFHs provide a richer parameter space featuring short-timescale variations of the SFR (burst and truncations) that are missing in exponentially declining (exp[-t/τ]) or delayed (t$\times$exp[-t/τ]) models (see also § 4.1).

4. RESULTS

4.1. *Stellar ages and SFHs*

The stellar age and SFH are not independent properties and thus, the chosen parametrization of the latter (single burst, N-bursts, τ models, SAMs, etc) often leads to strong degeneracies in the age and the characteristic timescale(s) of star formation (e.g., age-τ; Conroy 2013). These degeneracies, however, can be reduced using higher spectral-resolution datasets to probe features that are sensitive to different star-formation and quenching timescales (Kriek et al. 2011; Pérez-González et al. 2013; Belli et al. 2015).

Figure 4 illustrates the implications of assuming different SFHs to estimate the age of the galaxies. The blue shaded region shows the evolution of the sSFR and luminosity-weighted age vs. time for galaxies in the star-forming main sequence, as described by the SAM SFHs in the model library of Pacifici et al. (2012). Those galaxies are thought to be growing in a relatively smooth, secular mode (Elbaz et al. 2007; Rodighiero et al. 2010) in which gas inflow and SFR have reached a steady-state phase (e.g., Dekel et al. 2013). The main sequence pictured by SAM SFHs follows closely the observational results (e.g., Whitaker et al. 2014) which are also in good agreement with the predictions of other empirical models (e.g., Peng et al. 2010; Behroozi et al. 2013). In the main sequence paradigm, quenching can be interpreted as the departure from a stable growth phase, which can be either fast (e.g., SFR truncation; solid line) or slow (shallower slope; dashed line). After fast quenching, age increases linearly with time (i.e., passive evolution), while for slower quenching the slope is shallower, and the age increases slowly due to slowly declining star-formation (right panel of Figure 4). In τ models, the timescale controls the quenching time, and it can be tuned to describe fast or slow quenching (grey line in Figure 4). However, as one parameter characterizes the whole SFH, the prediction is not realistic for galaxies that are described by 2 or more distinct phases, such as a secular growth followed by fast quenching.

Panels a) and b) of Figure 5 show index-index diagrams sensitive to the SFH and quenching time. The colored

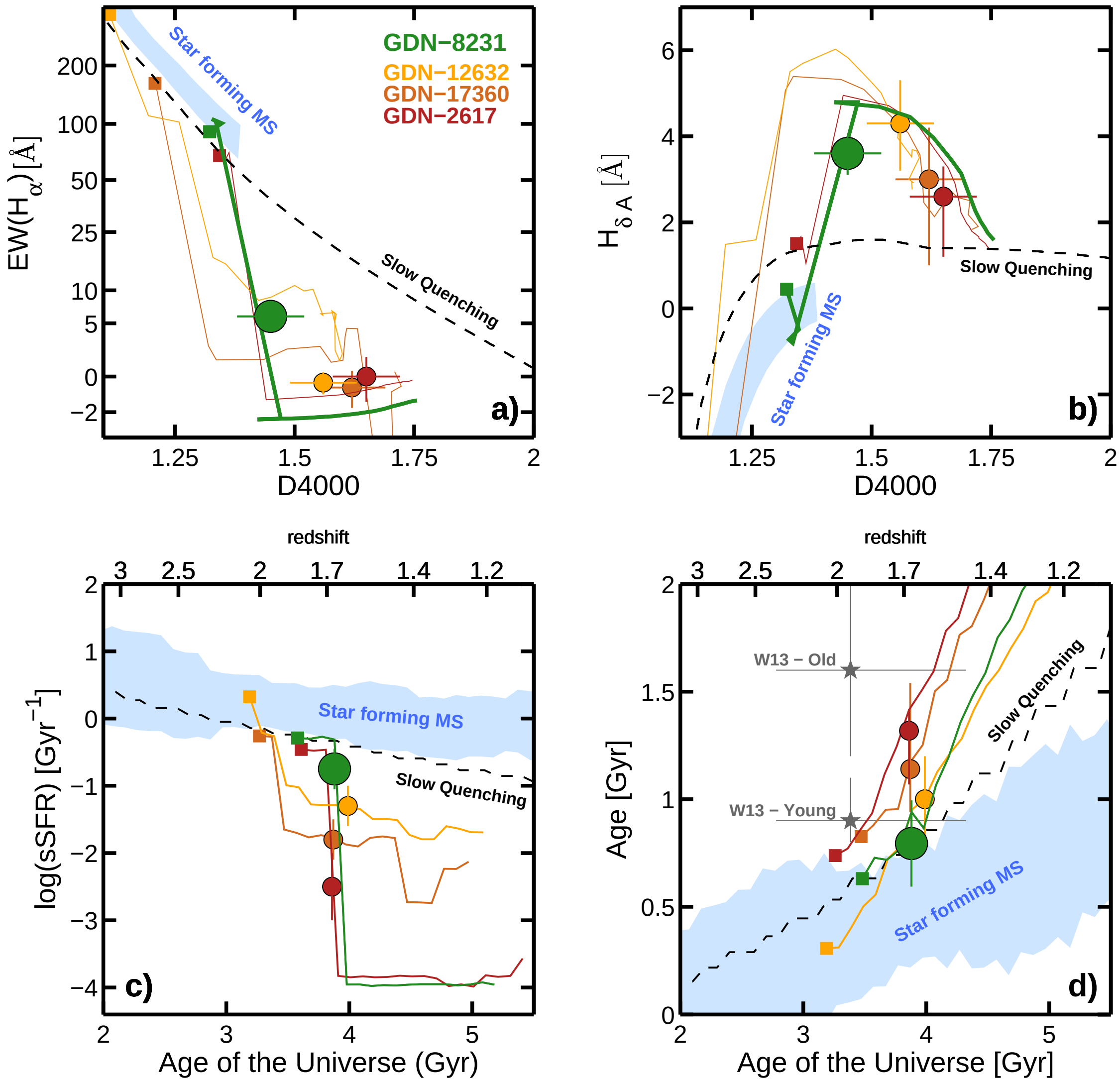

FIG. 5.— *Panels a) & b):* Index-index diagrams for the galaxies in the sample. The circles show the values measured in the spectra. The colors are the same as in Figure 1. The colored lines depict the evolutionary tracks for the best-fit SAM SFHs. The tracks start at the onset of quenching (colored squares) and continue for ∼1 Gyr after the redshift of observation. The blue shaded region and the dashed line show the evolution of the star-forming main sequence and the slow quenching galaxy depicted in Figure 4 and Panels c) and d). The Hα and Hδ indices are sensitive to recent changes in the SFR, while D4000 is a good tracer of the SFH averaged over longer timescales. In a fast quenching, the EW(Hα) drops abruptly while Hδ_A increases due to the appearance of prominent Balmer absorption lines. In contrast, a slow quenching galaxy has higher EW(Hα) and weaker Hδ_A for the same value of the D4000 index. *Panels c) & d):* Same as Figure 4 for the galaxies in our sample. The grey stars show the age of the oldest and youngest quiescent galaxies at $z \sim 2$ in Whitaker et al. 2013. All 4 galaxies are consistent with fast quenching. However, the details of the quenching path lead to different luminosity-weighted ages. For example, GDN-12632 was the first of quiescent galaxies to quench and is the youngest, while GDN-2617 was the last to quench and it is the oldest.

circles indicate the values measured in the MOSFIRE spectra of the 4 galaxies, and the lines show the evolutionary tracks of their best-fit SAM SFHs. The D4000 index is a good tracer of the average age of the stellar populations, while the EW(Hα) and Hδ_A are more sensitive to recent star-formation. For slow quenching, the EW(Hα) in emission decreases slowly while the Balmer absorption is relatively small and constant with time, Hδ_A ~ 1.8. In contrast, fast quenching causes a rapid decline in the Hα emission followed by an absorption plateau with EW(Hα)~ -2 Å, and a strong Hδ_A absorption. This relatively short-lived phase (∼1 Gyr), characterized by the lack of Hα emission and strong absorption in other Balmer lines, typical of A-stars, is known as a post-starburst phase (pSB; e.g., Wild et al. 2010).

The spectral properties of GDN-8231 agree well with the sSFR selection criteria indicating that the galaxy is on a fast quenching path. Besides the Hα emission, which indicates the presence of weak, ongoing star-formation, the SED fit, the D4000 index and the Hδ_A values suggest that the emission is rapidly declining. In fact, given the short quenching time, the chances of finding a galaxy in this phase are small, which makes GDN-8231 quite unique. The 3 quiescent galaxies in our sample are further along in their evolution, as indicated by their stronger D4000 ~ 1.6. However their indices and best-fit SFHs are also consistent with fast quenching. The similar SFHs are another indication that GDN-8231 is evolutionarily linked to the quenched galaxies. For a definition of quenching time, t_q, as the elapsed time from

having EW(Hα) values consistent with those of a main sequence galaxy, to EW(Hα)$\sim$ 0 (tracks in panel-a), the values range from a few Myrs for GDN-8231 (i.e., SFR truncation) to 500 Myr for GDN-17360. Interestingly the SAM SFHs suggest that galaxies show pSB features as a result of fast quenching from the star-forming main sequence, without being preceded by a strong starburst (i.e., $\sim$ 3$\times$ higher SFR than the main sequence). A more practical definition of $t_{\rm q}$ as the elapsed time from log(sSFR/Gyr^{-1})= 0 to -1 (tracks in panel c)), results in similar values of $t_{\rm q} = 300-800$ Myr.

The fast quenching scenario for all 4 galaxies agrees well with recent works that find strong Balmer absorptions on similarly young quiescent galaxies at $z \sim 1.5$ (Newman et al. 2010; Onodera et al. 2012; Bezanson et al. 2013; van de Sande et al. 2013; Belli et al. 2014a). It differs, however, with the results of Kriek et al. (2011), who studied a sample of stacked, high-resolution SEDs of galaxies at $0.5 < z < 2.0$ finding EW(Hα) values consistent with gradually declining SFHs. Assuming the difference is not caused by the slightly different redshift range, a plausible explanation for this discrepancy is that there are indeed different evolutionary quenching tracks (e.g., Martin et al. 2007; Gonçalves et al. 2012; Schawinski et al. 2014 or Belli et al. 2015), and current spectroscopic samples at $z \gtrsim 1.5$ are still not fully representative of the whole quenching population.

Panel d) of Figure 5 shows that the luminosity-weighted ages of the sample ranges from t$_w$ = 700 Myr for GDN-8231 to t$_w$ = 1.1 − 1.3 Gyr for the 3 quiescent galaxies. The SAM SFHs also suggest a formation redshift (i.e., onset of star formation) of $z_{\rm form} \gtrsim 6$, a half-mass assembly by $z \sim 3$ and the onset of quenching by $z \sim 2$. Interestingly, the latter is similar to the $z_{\rm form}$ of the galaxies inferred from τ models, which suggests a rapid build up ($\tau <$ 100 Myr). This, however, is most likely a limitation of single-parameter τ models, which are biased towards short values of τ in order to reproduce the strong pSB features in the SED. Secular SFHs with rise and decay timescales of several hundred Myr appear to be more realistic, and are predicted by physically motivated models (e.g., Peng et al. 2010; Behroozi et al. 2013; Gladders et al. 2013). However, obtaining a direct, reliable measurement of the formation timescale would require additional measurements such as the metallicity [Z/H] or the α element abundance [α/Fe], which trace the evolution of the metals (e.g., Conroy 2013; Onodera et al. 2014).

The stars in panel d) of Figure 5 show the age of the oldest, t$_w$= 1.5 Gyr, and youngest, t$_w$= 0.9 Gyr, quiescent galaxies at $z \sim 2$ from Whitaker et al. (2013) (see also Newman et al. 2013). The evolutionary tracks of the quiescent galaxies in our sample are consistent with being direct descendants of the youngest galaxies of Whitaker et al. (2013), and GDN-8231 reaches a similar age by $z = 1.5$. This implies that as new quenching galaxies join the red sequence the age spread in the quiescent population will increase by roughly 1 Gyr from $z = 2$ to $z = 1.5$. Interestingly, if all the galaxies in our sample follow a *pure* passive evolution since $z = 1.7$, their ages by $z = 0.6$ would be t$_w \sim 4.5-5$ Gyr, which is roughly 2 Gyr older than the results of Choi et al. (2014) for the oldest quiescent galaxies at that redshift. This could be an indication that some quiescent galaxies retain low levels of star formation, or perhaps experience minor wet mergers that rejuvenate star formation.

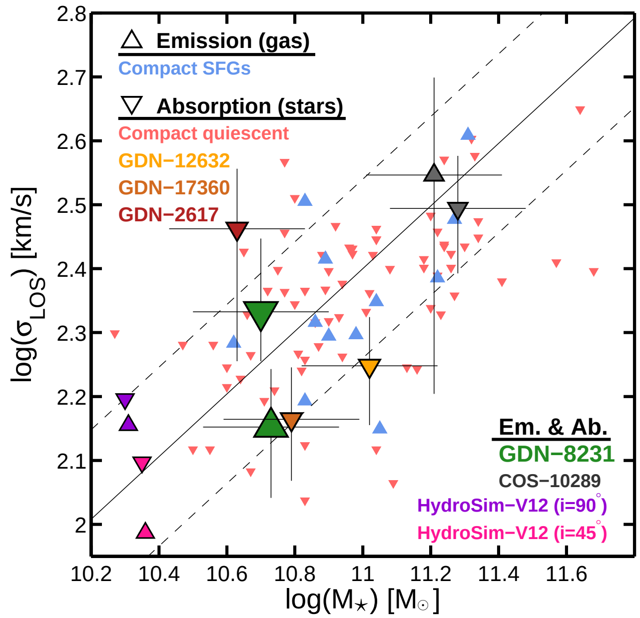

FIG. 6.— $\sigma_{\rm LOS}$ vs. M$_\star$ for different galaxy samples. The point up and down triangles show emission (gas) and absorption (stars) line measurements, respectively. The blue triangles depict 13 compact SFGs in Barro et al. (2014a), and one galaxy from Nelson et al. (2014). The red triangles show a compilation of quiescent galaxies (van de Sande et al. 2013; Bezanson et al. 2013; Belli et al. 2014a,b) at $z \gtrsim 1.5$. The overlapping distributions for compact SFGs and quiescent galaxies suggests that both populations have similar kinematic properties. This is supported by the agreement in the gas and stellar dispersions of COS-10289 (Belli et al. 2014b, and Barro et al. 2014b for the stellar and gas kinematics). However, GDN-8231 (green) has $\sim$ 40% lower dispersion in the gas than in the stars. A possible explanation is that the gas has colder kinematics than the stars ($v_\phi/\sigma_r > 1$), and thus its line-of-sight dispersion is prone to stronger projection effects. The gas and stellar dispersion for the simulated galaxy V12 (see also Figure 7) illustrates the bias towards lower values of $\sigma_{\rm LOS}^{\rm gas}$ with respect to $\sigma_{\rm LOS}^{\star}$ for viewing-angles closer to face-on (magenta).

In summary, the 4 galaxies in our sample have relatively young ages of t$_w \lesssim$ 1 Gyr and present spectral features consistent with fast quenching of the star formation. In particular, GDN-8231 seems to be caught in an early stage of a rapid truncation.

4.2. *Kinematic properties*

Figure 6 shows the M$_\star$−$\sigma_{\rm LOS}$ relation for a compilation of compact SFGs from Barro et al. (2014a) and quiescent galaxies at $z \gtrsim 1.5$ from the literature (van de Sande et al. 2013; Bezanson et al. 2013; Belli et al. 2014a,b). In Barro et al. (2014a), we found that 1) the gas kinematics of massive, compact SFGs are consistent with the stellar kinematics of compact quiescent galaxies, and 2) the dynamical masses of both populations are in good agreement with their stellar masses. We interpreted those similarities as evidence for an evolutionary connection. In particular, since both populations have similar structural, kinematic and dynamical properties, compact SFGs simply turn into compact quiescent galaxies by quenching their star formation. In addition, one galaxy (COS-10289), seemed to support this scenario

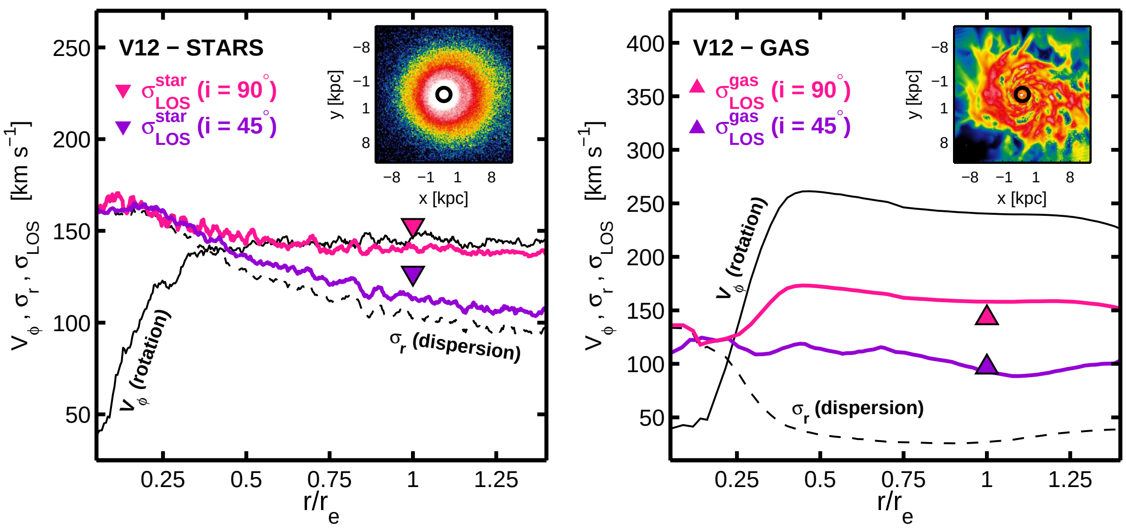

FIG. 7.— Stellar (left) and gas (right) kinematic profiles for the simulated galaxy V12 at $z = 2.3$ (Ceverino et al. 2014; Zolotov et al. 2014). The kinematic properties are measured in cylindrical beams with a depth of 8 kpc. The solid and dashed black lines depict the intrinsic rotation and dispersion. The magenta and purple lines show the $\sigma_{\rm LOS}$ profiles for a line-of-sight inclination of $i = 90°$ (edge-on) and $i = 45°$. The triangles show the integrated, mass-weighted values at the $r = r_{\rm e}$. The line-of-sight dispersion can be written as $\sigma^2_{\rm LOS} = \beta(\sin i\ v_\phi)^2 + \sigma_r^2$, where β depends on the inclination and density profile of the galaxy. This implies that for a rotation dominated component the value of $\sigma_{\rm LOS}$ depends more strongly on projection effects. In V12 the gas has higher rotation than the stars ($v_\phi/\sigma_r \sim 1.4$ vs. $v_\phi/\sigma_r \sim 5$) and therefore, the ratio of velocity dispersions can be as high as $\sigma^\star_{\rm LOS}/\sigma^{\rm gas}_{\rm LOS} \sim 1.5$ for a LOS inclination of $i = 45°$. The insets in the upper-right show the 10×10 kpc face-on density maps for the stars and the gas. The black circle has $r = r_{\rm e}$.

by showing agreement between its gas and stellar kinematics. However, the low S/N ratio of the emission line measurement and the presence of an X-ray AGN within the galaxy place caveats on the interpretation of the kinematic properties of the gas.

Quite surprisingly, the better-constrained measurements for GDN-8231 (green triangles in Figure 6) show that the gas has a lower velocity dispersion than the stars by a factor of $\sigma^\star_{\rm LOS}/\sigma^{\rm gas}_{\rm LOS} = 1.7 \pm 0.5$. Naively, we expected a value ~ 1 or, given that GDN-8231 is quenching, larger values of $\sigma^{\rm gas}_{\rm LOS}$ caused by strong feedback processes (e.g., shocks or outflows; Diamond-Stanic et al. 2012; Genzel et al. 2014). In turn, the smaller values of $\sigma^{\rm gas}_{\rm LOS}$ suggest that the gas is in dynamical equilibrium and that it has *colder* kinematic properties than the stars (i.e., higher v_ϕ/σ_r in the gas). If that is indeed the case, the lower dispersion in the gas could be the result of: 1) widespread star-formation activity in a disk observed at low inclination (i.e., close to edge-on), or 2) a centrally concentrated star-forming region probing, on average, lower values of the rotational velocity v_ϕ, which grows inside-out. As described in § 3.2, GDN-8231, has an inclination of $i = 42°$, and 20% smaller effective radius in the rest-frame NUV, which can lead to the smaller values of $\sigma^{\rm gas}_{\rm LOS}$ compared to $\sigma^\star_{\rm LOS}$.

In order to provide a better intuition, and quantify how much projection effects and/or a concentrated SFR profile affect the measurement of $\sigma_{\rm LOS}$, we study the kinematic profiles of the gas and the stars in V12, a high-resolution, hydrodynamic galaxy simulation (∼25 pc grid) drawn from the sample of Zolotov et al. (2014) and Ceverino et al. (2014). As described in Zolotov et al. (2014), these galaxies have similar stellar and structural evolution as the compact SFGs and therefore, V12 provides a excellent proxy for the analysis of the kinematic properties of GDN-8231. Figure 7 shows that the stars in V12 have comparable rotation and dispersion whereas the gas is rotation dominated (stellar $v_\phi/\sigma_r \sim 1.4$ vs. gas $v_\phi/\sigma_r \sim 5$). As a result, $\sigma^{\rm gas}_{\rm LOS}$ is more sensitive to projection effects and shows smaller values for low inclinations. For example, the integrated, mass-weighted $\sigma^{\rm gas}_{\rm LOS}$ at $r = r_{\rm e}$ show ratios of $\sigma^\star_{\rm LOS}/\sigma^{\rm gas}_{\rm LOS} \sim 1.0$ and 1.5 for an edge-on ($i = 90°$) and an intermediate inclination ($i = 45°$), respectively (see values in Figure 6). Therefore, we conclude that a large fraction of the observed ratio of velocity dispersions in GDN-8231 can be accounted for by projection effects.

On the other hand, given the relatively flat $\sigma^{\rm gas}_{\rm LOS}$ profile of V12 (right panel of Figure 7), the change in the integrated value of $\sigma^{\rm gas}_{\rm LOS}(r_{\rm e})$ would be small for a gas density (∝SFR) profile more centrally concentrated than the stellar profile (i.e., $r_{\rm e,\star} > r_{\rm e,gas}$). Using the ratio of effective radii in GDN-8231 ($r_{e,NUV}/r_{e,V} = 0.8$) as an example of different gas-to-stellar concentrations, we find that integrating $\sigma^{\rm gas}_{\rm LOS}$ only up $r = 0.8r_e$ decreases its value by less than 5% for the edge-on case. Nevertheless, the effect of the gas density profile in $\sigma^{\rm gas}_{\rm LOS}$ can be larger in GDN-8231 if: 1) it had a slowly-increasing rotation curve and a flat σ_r in the center, and/or 2) the emission line region, traced by Hα, had an even smaller $r_{\rm e}$ than the NUV luminosity profile. The latter is more plausible given the quenching nature of GDN-8231 and the shorter star-formation timescales probed by Hα.

Lastly, note that Figure 7 shows only the radial component of the intrinsic dispersion ($\sigma_{\rm r}$) for V12. In the case of anisotropic dispersion, for example due to strong collimated winds in the center of the galaxy ($\sigma_{\rm z} \gg \sigma_{\rm r}$), the observed value of $\sigma^{\rm gas}_{\rm LOS}$ for a face-on inclination would be much larger than that of $\sigma^\star_{\rm LOS}$.

4.2.1. *Dynamical mass*

We estimate the dynamical mass of GDN-8231 from $\sigma^\star_{\rm LOS}$ which, as described above, is less sensitive to projec-

tion effects. Following the virial equation:

$$M_{\rm dyn}(r<r_e) = K\frac{\sigma^2_{\rm LOS} r_e}{G} \quad (1)$$

where K depends on the galaxy's mass distribution, the inclination, and velocity field. We use $K = 2.5$, which is the most widely adopted value for stars in dispersion dominated galaxies (e.g., Newman et al. 2010; van de Sande et al. 2013; Belli et al. 2014b), and is valid under a variety of galaxy geometries and mass distributions (e.g., Binney & Tremaine 2008). We apply a small correction to scale the observed $\sigma^{\star}_{\rm LOS}$ to the value in a circular aperture of radius r_e, $\sigma_e = 1.05{\times}\sigma^{\star}_{\rm LOS}$ (Cappellari et al. 2006; van de Sande et al. 2011). The inferred dynamical mass $\log(\rm M_{dyn}/M_{\odot}) = 11.1$ is slightly larger than the stellar mass, but still consistent within the uncertainties in both the stellar mass and velocity dispersion. Previous works have reported a similar offset towards larger dynamical masses of $\log(M_{\rm dyn}/M_{\star}) = 0.1-0.16$ for recently quenched quiescent galaxies $z \gtrsim 1.5$ (Belli et al. 2014b).

5. CONCLUSIONS

We present Keck-I MOSFIRE NIR spectroscopy of GDN-8231, a massive, compact SFG galaxy at $z \sim 1.7$. This galaxy was selected with sSFR and rest-frame colors matching an intermediate stage between star-forming and quiescent. The Y and H band spectra reveal strong Balmer absorption lines and Hα and [N II] in emission. The emission and absorption lines yield spectral indices and the kinematics of the gas and the stars.

The spectral indices, SED-modeling, and the comparison to 3 compact quiescent galaxies at similar redshift, indicate that GDN-8231 was caught in a rare, early stage of fast quenching. Still relatively young, with a luminosity-weighted age of 700 ± 250 Myr, GDN-8231 will mature to become a compact quiescent galaxy by redshift $z = 1.5$. The rapid truncation of the SFR is evidenced by the low EW(Hα) and weak MIPS 24μm flux. The color profile is bluer in the center, which is consistent with the predictions of recent simulations for an early stage of inside-out quenching. The line ratio of [N II]/H$\alpha \sim 1$ suggests the presence of a weak (not X-ray detected) AGN, a common finding among most compact SFGs (Barro et al. 2014a). Using SFHs based on SAMs, we find that the assembly of GDN-8231 is consistent with an early ($z \sim 6$) onset of star-formation, a secular build-up in the star-forming main sequence, forming 50% of its stellar mass before $z = 3$, and fast quenching at $z \sim 1.7$.

In Barro et al. (2014b), we found that compact SFGs and quiescent galaxies have similar line-of-sight velocity dispersions for the gas and the stars, suggesting similar kinematics in progenitors and descendants. In GDN-8231, however, the dispersion of the gas, $\sigma^{\rm gas}_{\rm LOS}= 147 \pm 32$ km s^{-1}, is 40% smaller than that of the stars, $\sigma^{\star}_{\rm LOS}= 215 \pm 35$ km s^{-1}. This difference can be explained if the gas has colder kinematics (rotation dominated) than the stars, and therefore: a) $\sigma^{\rm gas}_{\rm LOS}$ is smaller if the viewing-angle is low (close to face-on), and b) $\sigma^{\rm gas}_{\rm LOS}$ is smaller if the emission-line (star-forming) region is concentrated at the center of the galaxy, and thus probes low values of v_{ϕ}. These options are consistent with the findings of state-of-the-art galaxy simulations which predict that the gas in compact SFGs reside in rotating disks (Zolotov et al. 2014). In the simulations, stars have $\sigma^{\star}_{\rm LOS}$ up to 1.5× larger depending on the projection of the gas disk. A clear prediction of these models is that the compact quiescent descendants should retain some rotation from its disky progenitors.

GDN-8231 stresses the need for larger samples of compact SFGs with emission and absorption line kinematics to quantify the effects predicted in the simulations. Those samples would allow us to study the dependence of $\sigma^{\star}_{\rm LOS}/\sigma^{\rm gas}_{\rm LOS}$ with the viewing-angle and star-formation activity. Similarly, high spatial resolution imaging in the sub-millimeter with ALMA, or in the NIR with adaptive optics, can provide direct measurements of the size and location of the star-forming regions and, in some cases, resolved kinematics for the ionized gas.

ACKNOWLEDGMENTS

Support for Program number HST-GO-12060 was provided by NASA through a grant from the Space Telescope Science Institute, which is operated by the Association of Universities for Research in Astronomy, Incorporated, under NASA contract NAS5-26555. GB acknowledges support from NSF grant AST-08-08133. PGP-G and MCEM acknowledge support from grant AYA2012-31277. JRT acknowledges support from NASA through Hubble Fellowship grant #51330. DC acknowledges support from AYA2012-32295. The simulations were performed at NASA Advanced Supercomputing (NAS) at NASA Ames Research Center. This work has made use of the Rainbow Cosmological Surveys Database, which is operated by the Universidad Complutense de Madrid (UCM), partnered with the University of California Observatories at Santa Cruz (UCO/Lick,UCSC). The authors recognize and acknowledge the very significant cultural role and reverence that the summit of Mauna Kea has always had within the indigenous Hawaiian community. We are most fortunate to have the opportunity to conduct observations from this mountain. Based partly on observations made with the Gran Telescopio Canarias (GTC), installed at the Spanish Observatorio del Roque de los Muchachos of the Instituto de Astrofsica de Canarias, in the island of La Palma.

REFERENCES

Alexander, D. M., Bauer, F. E., Brandt, W. N., et al. 2003, AJ, 126, 539
Baldwin, J. A., Phillips, M. M., & Terlevich, R. 1981, PASP, 93, 5
Balogh, M. L., Morris, S. L., Yee, H. K. C., Carlberg, R. G., & Ellingson, E. 1999, ApJ, 527, 54
Barro, G., Faber, S. M., Pérez-González, P. G., et al. 2013, ApJ, 765, 104
—. 2014a, ApJ, 791, 52
Barro, G., Trump, J. R., Koo, D. C., et al. 2014b, ArXiv e-prints
Bedregal, A. G., Scarlata, C., Henry, A. L., et al. 2013, ArXiv e-prints
Behroozi, P. S., Wechsler, R. H., & Conroy, C. 2013, ApJ, 770, 57
Belli, S., Newman, A. B., & Ellis, R. S. 2014a, ApJ, 783, 117
—. 2015, ApJ, 799, 206
Belli, S., Newman, A. B., Ellis, R. S., & Konidaris, N. P. 2014b, ApJ, 788, L29
Bezanson, R., van Dokkum, P., van de Sande, J., Franx, M., & Kriek, M. 2013, ApJ, 764, L8

TABLE 1
Stellar and spectroscopic properties of the MOSFIRE sample

ID (1)	R.A. (2)	DEC (3)	$z_{\rm spec}$ (4)	F160W (5)	log $M_\star$ (6)	r_e (7)	n (8)	$\sigma_\star$ (9)	$\sigma_{\rm gas}$ (10)	EW(Hα) (11)	H$\delta_{\rm A}$ (12)	D4000 (13)	Age (14)
8231	189.0656	62.1987	1.674	21.40	10.75	2.48	3.95	215±35	127±32	$5.9^{+1.1}_{-0.7}$	$3.6^{+0.5}_{-0.4}$	1.45±0.02	0.75±0.12
12632[a]	188.9625	62.2286	1.598	21.25	11.02	1.32	8.00	177±34	-	$-0.4^{+0.6}_{-0.8}$	$4.3^{+1.1}_{-1.0}$	1.59±0.03	1.07±0.20
17360	189.1153	62.2594	1.674	21.75	10.78	1.12	3.31	146±29	-	$-0.7^{+0.5}_{-1.1}$	$3.0^{+1.2}_{-2.0}$	1.62±0.03	1.14±0.15
2617	189.1003	62.1532	1.675	22.07	10.61	0.87	2.04	295±110	-	$0.0^{+0.5}_{-1.5}$	$2.6^{+0.7}_{-1.4}$	1.65±0.03	1.31±0.27

Note. —
(a) Observed in Newman et al. (2010); Belli et al. (2014a), LRIS optical spectroscopy with $\sigma = 174$km s^{-1}.
(1) General ID in the CANDELS H-band selected catalog in GOODS-N (Barro et al. in prep.) catalog.
(2,3) R.A and Declination J2000.
(4) Spectroscopic redshift.
(5) H band (F160W) magnitude.
(6) Stellar mass determined from SED fitting using Bruzual & Charlot (2003) and a Chabrier (2003) IMF, see § 2.1.
(7) Effective (half-light) radius (kpc) measured with GALFIT, see § 2.1.
(8) Sérsic index measured with GALFIT, see § 2.1.
(9) Integrated velocity dispersion (km s^{-1}) of the stars measured with PPXF (Cappellari & Emsellem 2004), see § 3.1.
(10) Integrated velocity dispersion (km s^{-1}) of the gas measured from the emission line width (FWHM), see § 3.1.
(11) Equivalent Width of Hα (Å) measured in the H band MOSFIRE spectra, see § 3.3.
(12) Spectral index H$\delta_{\rm A}$ (Å) measured in the Y band MOSFIRE spectra with PPXF, see § 3.3.
(13) D4000 index measured from the SED including broad- and medium- band photometry as well as *HST* grism spectroscopy, see § 3.3.
(14) Luminosity-weighted stellar age (Gyr) estimated from SED-fitting using the models of Pacifici et al. (2012).

Binney, J. & Tremaine, S. 2008, Galactic Dynamics: Second Edition (Princeton University Press)
Brammer, G. B., van Dokkum, P. G., & Coppi, P. 2008, ApJ, 686, 1503
Brammer, G. B., van Dokkum, P. G., Franx, M., et al. 2012, ApJS, 200, 13
Bruzual, G. & Charlot, S. 2003, MNRAS, 344, 1000
Buitrago, F., Trujillo, I., Conselice, C. J., et al. 2008, ArXiv e-prints
Calzetti, D., Armus, L., Bohlin, R. C., et al. 2000, ApJ, 533, 682
Cappellari, M., Bacon, R., Bureau, M., et al. 2006, MNRAS, 366, 1126
Cappellari, M. & Emsellem, E. 2004, PASP, 116, 138
Carollo, C. M., Bschorr, T. J., Renzini, A., et al. 2013, ApJ, 773, 112
Cassata, P., Giavalisco, M., Guo, Y., et al. 2011, ApJ, 743, 96
Cenarro, A. J., Peletier, R. F., Sánchez-Blázquez, P., et al. 2007, MNRAS, 374, 664
Ceverino, D., Dekel, A., & Bournaud, F. 2010, MNRAS, 404, 2151
Ceverino, D., Klypin, A., Klimek, E. S., et al. 2014, MNRAS, 442, 1545
Chabrier, G. 2003, PASP, 115, 763
Cheung, E., Faber, S. M., Koo, D. C., et al. 2012, ArXiv e-prints
Choi, J., Conroy, C., Moustakas, J., et al. 2014, ApJ, 792, 95
Cimatti, A., Cassata, P., Pozzetti, L., et al. 2008, A&A, 482, 21
Conroy, C. 2013, ARA&A, 51, 393
Conroy, C. & Gunn, J. E. 2010, ApJ, 712, 833
Daddi, E., Renzini, A., Pirzkal, N., et al. 2005, ApJ, 626, 680
Damjanov, I., McCarthy, P. J., Abraham, R. G., et al. 2009, ApJ, 695, 101
Dekel, A., Birnboim, Y., Engel, G., et al. 2009, Nature, 457, 451
Dekel, A. & Burkert, A. 2014, MNRAS, 438, 1870
Dekel, A., Zolotov, A., Tweed, D., et al. 2013, MNRAS, 435, 999
Diamond-Stanic, A. M., Moustakas, J., Tremonti, C. A., et al. 2012, ApJ, 755, L26
Elbaz, D., Daddi, E., Le Borgne, D., et al. 2007, A&A, 468, 33
Elbaz, D., Dickinson, M., Hwang, H. S., et al. 2011, A&A, 533, A119
Falcón-Barroso, J., Sánchez-Blázquez, P., Vazdekis, A., et al. 2011, A&A, 532, A95
Fang, J. J., Faber, S. M., Koo, D. C., & Dekel, A. 2013, ApJ, 776, 63
Galametz, A., Grazian, A., Fontana, A., et al. 2013, ApJS, 206, 10
Genzel, R., Förster Schreiber, N. M., Rosario, D., et al. 2014, ArXiv e-prints
Gladders, M. D., Oemler, A., Dressler, A., et al. 2013, ApJ, 770, 64
Gonçalves, T. S., Martin, D. C., Menéndez-Delmestre, K., Wyder, T. K., & Koekemoer, A. 2012, ApJ, 759, 67
Grogin, N. A., Kocevski, D. D., Faber, S. M., et al. 2011, ApJS, 197, 35
Guo, Y., Ferguson, H. C., Giavalisco, M., et al. 2013, ApJS, 207, 24
Guo, Y., Giavalisco, M., Cassata, P., et al. 2012, ApJ, 749, 149
Hernán-Caballero, A., Alonso-Herrero, A., Pérez-González, P. G., et al. 2014, MNRAS, 443, 3538
Hopkins, P. F., Hernquist, L., Cox, T. J., et al. 2006, ApJS, 163, 1
Kauffmann, G., Heckman, T. M., Tremonti, C., et al. 2003, MNRAS, 346, 1055
Kelson, D. D., Illingworth, G. D., Franx, M., & van Dokkum, P. G. 2001, ApJ, 552, L17
Kennicutt, Jr., R. C. 1998, ARA&A, 36, 189
Koekemoer, A. M., Faber, S. M., Ferguson, H. C., et al. 2011, ApJS, 197, 36
Kriek, M., Shapley, A. E., Reddy, N. A., et al. 2014, ArXiv e-prints
Kriek, M., van Dokkum, P. G., Labbé, I., et al. 2009, ApJ, 700, 221
Kriek, M., van Dokkum, P. G., Whitaker, K. E., et al. 2011, ApJ, 743, 168
Liu, F. S., Guo, Y., Koo, D. C., et al. 2013, ApJ, 769, 147
Magdis, G. E., Rigopoulou, D., Huang, J.-S., & Fazio, G. G. 2010, MNRAS, 401, 1521
Martin, D. C., Wyder, T. K., Schiminovich, D., et al. 2007, ApJS, 173, 342
McLean, I. S., Steidel, C. C., Epps, H., et al. 2010, in Society of Photo-Optical Instrumentation Engineers (SPIE) Conference Series, Vol. 7735, Society of Photo-Optical Instrumentation Engineers (SPIE) Conference Series
McLean, I. S., Steidel, C. C., Epps, H. W., et al. 2012, in Society of Photo-Optical Instrumentation Engineers (SPIE) Conference Series, Vol. 8446, Society of Photo-Optical Instrumentation Engineers (SPIE) Conference Series
Miller, S. H., Bundy, K., Sullivan, M., Ellis, R. S., & Treu, T. 2011, ApJ, 741, 115
Muzzin, A., Marchesini, D., van Dokkum, P. G., et al. 2009, ApJ, 701, 1839
Naab, T., Johansson, P. H., Ostriker, J. P., & Efstathiou, G. 2007, ApJ, 658, 710
Nelson, E., van Dokkum, P., Franx, M., et al. 2014, Nature, 513, 394
Newman, A. B., Ellis, R. S., Andreon, S., et al. 2013, ArXiv e-prints
Newman, A. B., Ellis, R. S., Bundy, K., & Treu, T. 2012a, ApJ, 746, 162
Newman, A. B., Ellis, R. S., Treu, T., & Bundy, K. 2010, ApJ, 717, L103

Newman, S. F., Genzel, R., Förster-Schreiber, N. M., et al. 2012b, ApJ, 761, 43
Noeske, K. G., Weiner, B. J., Faber, S. M., et al. 2007, ApJ, 660, L43
Onodera, M., Carollo, C. M., Renzini, A., et al. 2014, ArXiv e-prints
Onodera, M., Renzini, A., Carollo, M., et al. 2012, ApJ, 755, 26
Pacifici, C., Charlot, S., Blaizot, J., & Brinchmann, J. 2012, MNRAS, 421, 2002
Pacifici, C., da Cunha, E., Charlot, S., et al. 2014, ArXiv e-prints
—. 2015, MNRAS, 447, 786
Pannella, M., Carilli, C. L., Daddi, E., et al. 2009, ApJ, 698, L116
Pannella, M., Elbaz, D., Daddi, E., et al. 2014, ArXiv e-prints
Patel, S. G., van Dokkum, P. G., Franx, M., et al. 2013, ArXiv e-prints
Peng, Y.-j., Lilly, S. J., Kovač, K., et al. 2010, ApJ, 721, 193
Pérez-González, P. G., Cava, A., Barro, G., et al. 2013, ApJ, 762, 46
Price, S. H., Kriek, M., Brammer, G. B., et al. 2014, ApJ, 788, 86
Rodighiero, G., Cimatti, A., Gruppioni, C., et al. 2010, A&A, 518, L25
Salim, S., Rich, R. M., Charlot, S., et al. 2007, ApJS, 173, 267
Sánchez-Blázquez, P., Gorgas, J., Cardiel, N., & González, J. J. 2006a, A&A, 457, 787
Sánchez-Blázquez, P., Peletier, R. F., Jiménez-Vicente, J., et al. 2006b, MNRAS, 371, 703
Schawinski, K., Urry, C. M., Simmons, B. D., et al. 2014, MNRAS, 440, 889
Stefanon, M., Marchesini, D., Rudnick, G. H., Brammer, G. B., & Whitaker, K. E. 2013, ApJ, 768, 92
Szomoru, D., Franx, M., & van Dokkum, P. G. 2012, ApJ, 749, 121
Toft, S., Gallazzi, A., Zirm, A., et al. 2012, ApJ, 754, 3
Trager, S. C., Faber, S. M., Worthey, G., & González, J. J. 2000, AJ, 119, 1645
Trujillo, I., Conselice, C. J., Bundy, K., et al. 2007, MNRAS, 382, 109
Trump, J. R., Konidaris, N. P., Barro, G., et al. 2013, ApJ, 763, L6
van de Sande, J., Kriek, M., Franx, M., et al. 2013, ApJ, 771, 85
—. 2011, ApJ, 736, L9
van der Wel, A., Franx, M., van Dokkum, P. G., et al. 2014, ApJ, 788, 28
van Dokkum, P. G., Bezanson, R., van der Wel, A., et al. 2014, ApJ, 791, 45
van Dokkum, P. G. & Brammer, G. 2010, ApJ, 718, L73
van Dokkum, P. G., Franx, M., Kriek, M., et al. 2008, ApJ, 677, L5
Wellons, S., Torrey, P., Ma, C.-P., et al. 2014, ArXiv e-prints
Whitaker, K. E., Franx, M., Leja, J., et al. 2014, ApJ, 795, 104
Whitaker, K. E., Kriek, M., van Dokkum, P. G., et al. 2012a, ApJ, 745, 179
Whitaker, K. E., Labbé, I., van Dokkum, P. G., et al. 2011, ApJ, 735, 86
Whitaker, K. E., van Dokkum, P. G., Brammer, G., & Franx, M. 2012b, ApJ, 754, L29
Whitaker, K. E., van Dokkum, P. G., Brammer, G., et al. 2013, ArXiv e-prints
Wild, V., Almaini, O., Cirasuolo, M., et al. 2014, MNRAS, 440, 1880
Wild, V., Heckman, T., & Charlot, S. 2010, MNRAS, 405, 933
Williams, R. J., Quadri, R. F., Franx, M., et al. 2010, ApJ, 713, 738
Worthey, G. & Ottaviani, D. L. 1997, ApJS, 111, 377
Wuyts, S., Cox, T. J., Hayward, C. C., et al. 2010, ApJ, 722, 1666
Wuyts, S., Förster Schreiber, N. M., Lutz, D., et al. 2011a, ApJ, 738, 106
Wuyts, S., Förster Schreiber, N. M., van der Wel, A., et al. 2011b, ApJ, 742, 96
Wuyts, S., Labbé, I., Franx, M., et al. 2007, ApJ, 655, 51
Yesuf, H. M., Faber, S. M., Trump, J. R., et al. 2014, ApJ, 792, 84
Zolotov, A., Dekel, A., Mandelker, N., et al. 2014, ArXiv e-prints